Compact Mach–Zehnder Interferometer Based on Tapered Hollow Optical Fiber

Cong-Cong Zhu, Yong-Sen Yu, Xuan-Yu Zhang, Chao Chen, Ju-Fa Liang, Zi-Jian Liu, Ai-Hua Meng, Shi-Mei Jing, and Hong-Bo Sun, *Member, IEEE*

Abstract—A compact fiber Mach–Zehnder interferometer based on tapered hollow optical fiber (THOF) has been demonstrated. The THOF is sandwiched between two single mode fibers (SMFs), forming a SMF-THOF-SMF (STS) structure. The discharging during the splicing and tapering processes induces the collapsed regions in the hollow fiber, which form the modal coupling/re-coupling areas of the interferometer. The THOF has a length of about 2 mm and the taper waist diameter is about 66.5 μm. The refractive index (RI), stress, and temperature response properties of the STS interferometer have been investigated, which show a high RI sensitivity and low temperature cross-sensitivity. The STS interferometer holds the merits of compact structure, low cost and easy fabrication, making it a suitable candidate in the biochemical and physical sensing fields.

Index Terms—Fiber optical sensor, Mach-Zehnder interferometer, hollow optical fiber, fiber taper.

I. INTRODUCTION

AS AN important component of fiber optical sensors (such as fiber gratings [1]–[3] and fiber modal interferometers [4]), fiber Mach-Zehnder interferometer (MZI) possesses the common advantages of the fiber sensors, namely, simple configuration, fast response, light weight and electromagnetic immunity. In recent years, in order to pursue the aims of high sensitivity, compact structure and ease of fabrication, various methods have been developed to fabricate MZIs with fibers in different fiber categories. Compared with femtosecond laser [5] and CO_2 laser machining [6], the splicing and tapering methods show the merits of low cost and high fabrication efficiency. As an effective approach to fabricate MZIs through splicing, the single mode fiber (SMF)-multimode fiber (MMF)-single mode fiber structures [7], [8] have been investigated for years and have been employed to realize many interferometers with novel characteristics. However, the long MMF regions in such structures make the sensors difficult to be packaged and to realize localized
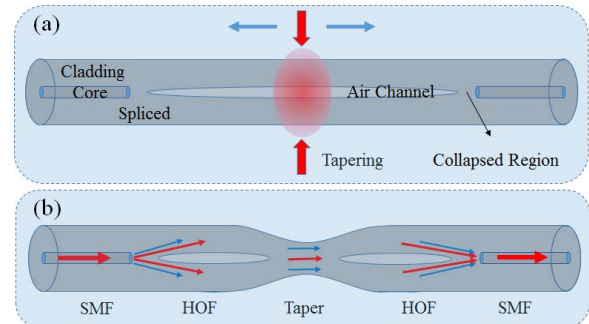
Fig. 1. Schematic diagram of the fabrication process (a) and the interference principle (b) of the STS interferometer fabricated by the splicing and tapering procedures with fiber fusion splicer.

sensing. On the other hand, the MZIs fabricated in SMFs by core offset splicing [9], tapering [10] or waist enlarging [11] usually suffer from the similar problems. In addition, photonic crystal fibers or other special fibers have also been used to realize the MZIs, but they are costly [12], [13] and the refractive index (RI) sensitivity needs to be further improved [14], [15].

Hollow optical fiber (HOF), which is a hollow silica tube with air inside, has attracted a lot of attention in recent years. Several MZIs [16], [17] based on the HOF have been reported. Nevertheless, they have a significant temperature dependence; meanwhile, they need special care during the splicing process to improve the interference visibility and to ensure the mechanical strength at the splicing interface.

In this letter, we demonstrate the fabrication of a MZI by sandwiching a tapered hollow optical fiber (THOF) between two segments of SMFs, then the interferometer has the SMF-THOF-SMF (STS) structure. The splicing and tapering regions of the sensor are collapsed because of heat effect. The RI, stress and temperature response characteristics of different peaks of the STS interferometer are investigated. For the interference peak at around 1440 nm, a maximum RI sensitivity of 7041.21 nm/RI unit (RIU) is achieved in the RI range of 1.4406~1.4458, as well as a stress sensitivity of -6.26 nm/N in the stress range of 0~1 N and a low temperature sensitivity of 9.8 pm/°C in the temperature range of 30 °C~100 °C.

II. EXPERIMENTS

The fabrication process of the STS interferometer is illustrated in Fig. 1(a). Firstly, a segment of

SMF (SMF-28e, Corning) and a segment of HOF were cleaved, and then spliced together by a commercial fusion splicer (FSU-975, Ericsson) with the built-in SMF splicing program. A collapsed region with the length of about 400 μm, which was composed of silica, was created at the interface between the SMF and HOF during the splicing process. The SMF has a core diameter of 8.2 μm and a cladding diameter of 125 μm, and it has a cut-off wavelength of 1260 nm. The HOF has an air channel and a silica cladding with diameters of about 10 μm and 126 μm, respectively. The polyimide coating of the HOF with a thickness of about 12 μm was stripped off in the experiment. After the stripping, the HOF can be regarded as a waveguide with the surrounding medium as the cladding. Secondly, the HOF was cleaved by a high precision fiber cleaver with a distance of about 2 mm away from the collapsed region. It was then spliced with another segment of SMF. After the splicing, the two pigtails of the fabricated device were connected to a supercontinuum broadband source (BBS) (Superk Compact, NKT Photonics) and an optical spectrum analyzer (OSA) (AQ6370, Yokogawa), respectively. The BBS has a bandwidth of 1900 nm ranging from 500 nm to 2400 nm, and the OSA has a maximum wavelength resolution of 0.02 nm. Finally, the fabricated device was tapered in the middle of the hollow fiber by the fusion splicer with a discharging current of 11 mA and a tapering time of 12 s, which could affect the extinction ratio of the interference peaks in the transmission spectrum. During the tapering process, the transmission spectrum was monitored by the OSA.

When the light guided in the SMF core is transmitted to the HOF, due to the collapsed region between the SMF and HOF, the light will be mainly coupled to the silica region of the HOF and guided along the silica region instead of being confined in the central air channel. The fabricated STS structure can induce the interference between fundamental mode and high-order mode of the HOF. The two collapsed regions around the splicing interfaces play the roles of splitting and combining couplers, as illustrated in Fig. 1(b). At the first collapsed region, the core mode of the lead-in SMF is split into the fundamental mode and high-order modes of the HOF; at the second collapsed region, the split modes are recombined into the lead-out SMF. While in the taper region, the fundamental mode of the HOF will be partly coupled to the high-order mode that the power of modes participating in the interference will be more matched and the mode interference will be enhanced [18]. Thus, a transmission spectrum with high extinction ratio can be achieved after tapering with a proper tapering time and discharging current.

The microscope image of the fabricated STS interferometer is shown in Fig. 2(a), where the collapsed regions at the interfaces between the SMF and HOF are not fully displayed. The air channels remaining in the HOF are 454.1 μm and 421.3 μm in length, respectively. The collapsed region formed in the tapering process is about 302.9 μm, which has been turned into a whole silica region. The diameter of the taper waist is 66.5 μm, which indicates that the fabricated structure could still keep a relatively high mechanical strength. A smaller taper waist diameter could improve the
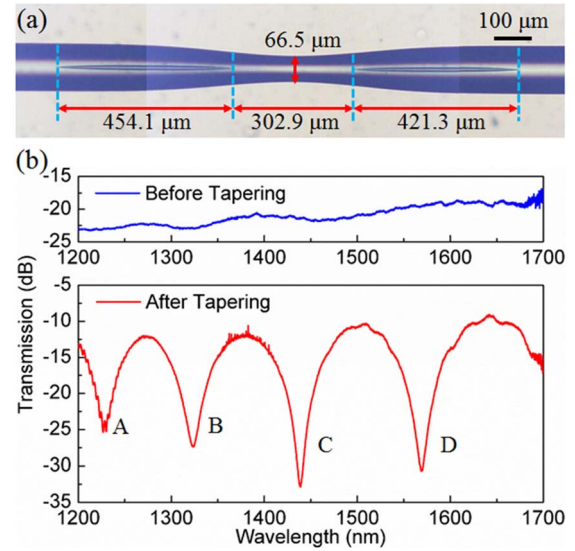

Fig. 2. (a) Optical microscope image of the fabricated STS interferometer. (b) The transmission spectra of the fabricated device before and after tapering.

RI sensing sensitivity because the evanescent field of the travelling light is stronger [19], however, it will reduce the mechanical strength of the sensor. Considering the factors of extinction ratio, sensitivity and mechanical strength, we chose the above tapering time and discharging current to fabricate the taper in the experiment. The spectrum before tapering is presented in Fig. 2(b), in which no obvious resonance peaks are observed in the wavelength range from 1200 nm to 1700 nm. The loss is about 22 dB, which mainly comes from the scattering in the collapsed regions at the SMF and HOF interfaces and the attenuation when propagating along the silica tube. After tapering, a quasi-sine interference spectrum is achieved, as shown in Fig. 2(b). Meanwhile, some other high-order modes are also produced, which participate in the interference and slightly modify the envelope of the interference spectrum. The insertion loss of the fabricated sensor is about 11 dB, which is about 2 times smaller than those obtained in refs. [17] and [20], comparable to those in refs. [6], [11], and [16], and about 10 times larger than that in ref. [10].

The spectrum characteristics of the STS interferometer can be described with the two beam interference model [11],

$$I = I_1 + I_2 + 2\sqrt{I_1 I_2} \cos[\frac{2\pi \, \Delta n_{eff} L}{\lambda}] \qquad (1)$$

where I is the output light intensity, I_1 and I_2 are the intensity of the fundamental mode and high-order mode of the HOF participating in the interference, respectively. $\Delta n_{eff} = n_1 - n_2$ is the difference of the effective RI between the modes. L is the length of the interferometer and λ is the input light wavelength. According to Eq. (1), the highest extinction ratio will be achieved when I_1 equals to I_2.

The free spectral range (FSR) of the fabricated STS interferometer can be determined by,

$$FSR = \lambda^2 / \Delta n_{eff} L \qquad (2)$$

The FSR at around 1500 nm is about 130 nm. Considering that the length of the HOF spliced between the SMFs is
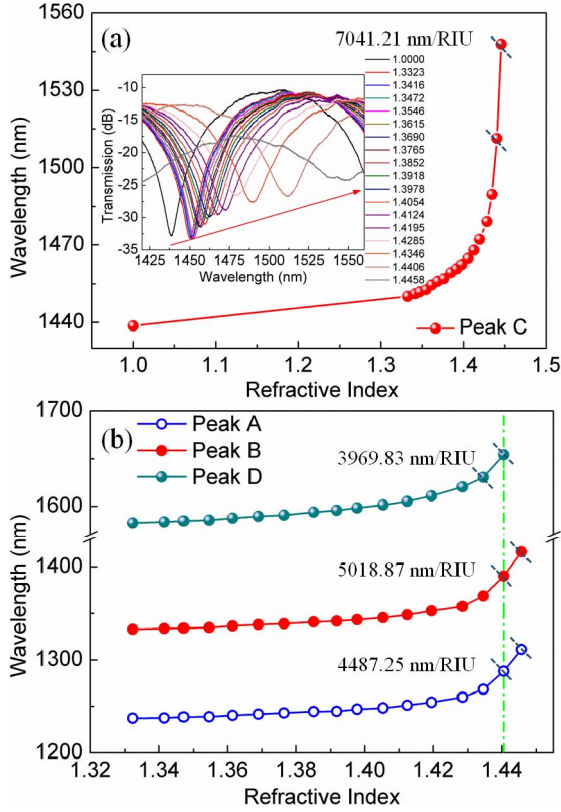
Fig. 3. (a) The wavelength of the peak C changes with the surrounding RI. Inset: the spectrum evolution with the increase of RI and the red arrow represents the RI increase. (b) The wavelength response curves of the other peaks with the increase of RI.

about 2 mm, the Δn_{eff} is calculated to be about 0.009. This indicates that the modes participating in the interference should not propagate in different media as the silica tube and the air have a RI difference of about 0.44.

III. SENSING CHARACTERISTICS AND DISCUSSIONS

To investigate the surrounding RI response characteristics of the fabricated sensor, the STS interferometer was fixed on a piece of glass slide to keep it straight. The water-glycerin RI solutions were added to the glass slide to immerse the whole STS sensor. The RI solutions, which were calibrated by an Abbe refractometer, were in the RI range of 1.3323∼1.4458. After each test, the STS interferometer was cleaned by ethanol and deionized water to recover its initial spectrum in air. The responses of different peaks of the sensor to surrounding RIs were investigated. The wavelength shift was read by the OSA with the 3-dB central wavelength of the interference peak. The response curve of the peak C to different RIs is shown in Fig. 3(a), in which a maximum sensitivity of 7041.21 nm/RIU is achieved in the RI range of 1.4406∼1.4458. The spectrum evolution with the RI increase is shown in the inset of Fig. 3(a), which presents a red-shift of the wavelength. As the surrounding RI further increases, the RI will be equal to the effective index of the high-order mode and the interference peak will be weakened. The response curves of the peaks A, B and D are shown in Fig. 3(b), the maximum sensitivities of which equal
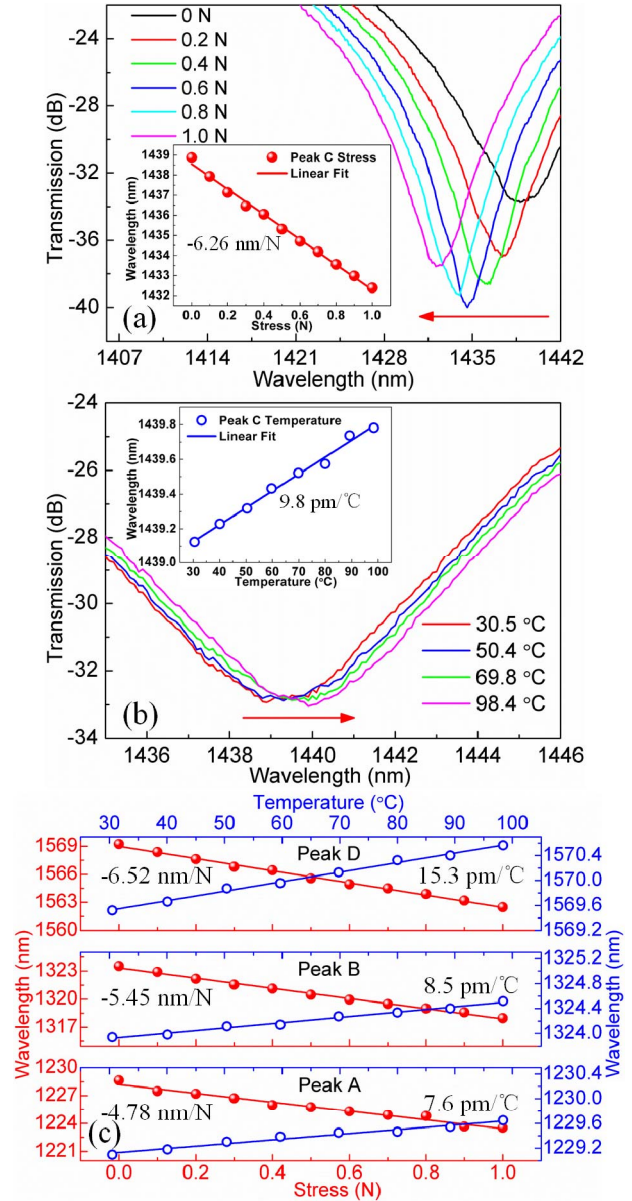

Fig. 4. (a)-(b) The spectrum shift of the peak C when the STS interferometer is applied to different stresses and temperatures, respectively. The red arrow represents the increase of stress and temperature. Inserts: measurement results and linear fit of the results. (c) Linear fit of the measurement results of the peaks A, B and D. The solid dots (hollow circles) and red (blue) line represent the stress (temperature) response, respectively.

to 4487.25 nm/RIU, 5018.87 nm/RIU and 3969.83 nm/RIU, respectively. The maximum sensitivity of the peak D could be higher, but the peak D in the higher RI region shifts beyond the wavelength detection range of the OSA. In the RI range of 1.3416∼1.3918, the sensor shows a linear response to the surrounding RI, where the peak C shows a high RI sensitivity of 202.48 nm/RIU. It is about 10 times larger than that obtained in ref. [19], 8 times larger than those in refs. [10] and [15], and similar to that in ref. [20]. The RI sensitivities of the other three peaks in this RI range are 160.45 nm/RIU, 173.68 nm/RIU and 257.41 nm/RIU, respectively. In the RI range of 1.3918∼1.4406, the four peaks show an exponential response and the sensitivities

are in the range of 170.83 nm/RIU $\sim$ 3257.62 nm/RIU, 257.90 nm/RIU $\sim$ 3569.92 nm/RIU, 287.03 nm/RIU $\sim$ 3594.50 nm/RIU and 423.75 nm/RIU $\sim$ 3969.83 nm/RIU, respectively.

The stress response mesurement of the sensor was conducted by moving one fiber clamp against the other one, which was connected to a piezoelectric tensometer. The applied stress is in the range of 0$\sim$1 N with an increasing step of 0.1 N. The spectrum evolution of the peak C as a function of the stress is shown in Fig. 4(a). The stress response is shown by the solid dots in the inset of Fig. 4(a), which demonstrates a stress sensitivity of about -6.26 nm/N. The sensitivity is comparable to that obtained in ref. [20] and about 30 times smaller than that in ref. [21]. As shown in Fig. 4(c), the stress sensitivities of the peaks A, B and D are -4.78 nm/N, -5.45 nm/N and -6.52 nm/N, respectively.

By placing the fabricated STS interferometer in a digitally controlled tube furnace, we investigated the temperature response characteristics of the sensor from 30 °C to 100 °C with an increasing step of 10 °C. As shown in Fig. 4(b), the peak C has a red-shift as the temperature increases. From the linear fit of the measurement results in the inset of Fig. 4(b), the peak C shows a low temperature sensitivity of about 9.8 pm/°C, which is about 11 times smaller than that obtained in ref. [5], about 8 times smaller than those in refs. [6], [8], and [10], and about 5 times smaller than those in refs. [7] and [16]. It indicates that the sensor has a low temperature cross-sensitivity, as for peak C, the temperature cross-sensitivities for high RI and stress are about 1.39×10^{-6} RIU/°C and 1.57×10^{-3} N/°C, respectively. The temperature influence could be neglected for some applications, where we could only detect one peak to measure RI or stress. In such cases, we could use an optical source with narrower bandwidth and reduce the scanning time of the OSA. The temperature sensitivities of the other three peaks are 7.6 pm/°C, 8.5 pm/°C and 15.3 pm/°C, respectively, which are illustrated in Fig. 4(c).

IV. Conclusion

In conclusion, a STS interferometer was demonstrated in this letter by sandwiching a segment of THOF between the SMFs. The surrounding RI, stress and temperature response characteristics of the STS interferometer were investigated. The sensor demonstrated a high RI sensitivity of about 7041.21 nm/RIU in the range of 1.4406$\sim$1.4458, a stress sensitivity of -6.26 nm/N in the range of 0$\sim$1 N and a low temperature sensitivity of 9.8 pm/°C in the range of 30 °C$\sim$100 °C for the peak located around 1440 nm. The proposed sensor can also be used for simultaneous measurement of RI, stress and temperature by monitoring different interference peaks, such as the three peaks above the cut-off wavelength of the SMF.

References

[1] C. Chen et al., "Monitoring thermal effect in femtosecond laser interaction with glass by fiber Bragg grating," *J. Lightw. Technol.*, vol. 29, no. 14, pp. 2126–2130, Jul. 15, 2011.

[2] S. W. James, S. Korposh, S. W. Lee, and R. P. Tatam, "A long period grating-based chemical sensor insensitive to the influence of interfering parameters," *Opt. Exp.*, vol. 22, no. 7, pp. 8012–8023, Apr. 2014.

[3] W. Xiong et al., "Simultaneous additive and subtractive three-dimensional nanofabrication using integrated two-photon polymerization and multiphoton ablation," *Light, Sci. Appl.*, vol. 1, p. e6, Apr. 2012.

[4] Z. Tian, S. S.-H. Yam, and H.-P. Loock, "Refractive index sensor based on an abrupt taper Michelson interferometer in a single-mode fiber," *Opt. Lett.*, vol. 33, no. 10, pp. 1105–1107, May 2008.

[5] L. Jiang, J. Yang, S. Wang, B. Li, and M. Wang, "Fiber Mach–Zehnder interferometer based on microcavities for high-temperature sensing with high sensitivity," *Opt. Lett.*, vol. 36, no. 19, pp. 3753–3755, Oct. 2011.

[6] T. Wei, X. Lan, and H. Xiao, "Fiber inline core–cladding-mode Mach–Zehnder interferometer fabricated by two-point CO_2 laser irradiations," *IEEE Photon. Technol. Lett.*, vol. 21, no. 10, pp. 669–671, May 15, 2009.

[7] Y. Liu and L. Wei, "Low-cost high-sensitivity strain and temperature sensing using graded-index multimode fibers," *Appl. Opt.*, vol. 46, no. 13, pp. 2516–2519, May 2007.

[8] M. Shao, X. Qiao, H. Fu, H. Li, Z. Jia, and H. Zhou, "Refractive index sensing of SMS fiber structure based Mach–Zehnder interferometer," *IEEE Photon. Technol. Lett.*, vol. 26, no. 5, pp. 437–439, Mar. 1, 2014.

[9] Z. Tian, S. S.-H. Yam, and H.-P. Loock, "Single-mode fiber refractive index sensor based on core-offset attenuators," *IEEE Photon. Technol. Lett.*, vol. 20, no. 16, pp. 1387–1389, Aug. 15, 2008.

[10] P. Lu, L. Men, K. Sooley, and Q. Chen, "Tapered fiber Mach–Zehnder interferometer for simultaneous measurement of refractive index and temperature," *Appl. Phys. Lett.*, vol. 94, no. 13, pp. 131110-1–131110-3, Mar. 2009.

[11] Y. Geng, X. Li, X. Tan, Y. Deng, and Y. Yu, "High-sensitivity Mach–Zehnder interferometric temperature fiber sensor based on a waist-enlarged fusion bitaper," *IEEE Sensors J.*, vol. 11, no. 11, pp. 2891–2894, Nov. 2011.

[12] J. Villatoro, V. P. Minkovich, V. Pruneri, and G. Badenes, "Simple all-microstructured-optical-fiber interferometer built via fusion splicing," *Opt. Exp.*, vol. 15, no. 4, pp. 1491–1496, Feb. 2007.

[13] C. Shen et al., "Polarization-dependent curvature sensor based on an in-fiber Mach–Zehnder interferometer with a difference arithmetic demodulation method," *Opt. Exp.*, vol. 20, no. 14, pp. 15406–15417, Jul. 2012.

[14] Y. Zhang et al., "Simultaneous measurement of temperature and curvature based on hollow annular core fiber," *IEEE Photon. Technol. Lett.*, vol. 26, no. 11, pp. 1128–1131, Jun. 1, 2014.

[15] F. Pang et al., "In-fiber Mach–Zehnder interferometer based on double cladding fibers for refractive index sensor," *IEEE Sensors J.*, vol. 11, no. 10, pp. 2395–2400, Oct. 2011.

[16] Y. Jung, S. Lee, B. H. Lee, and K. Oh, "Ultracompact in-line broadband Mach–Zehnder interferometer using a composite leaky hollow-optical-fiber waveguide," *Opt. Lett.*, vol. 33, no. 24, pp. 2934–2936, Dec. 2008.

[17] D.-W. Duan et al., "In-fiber Fabry–Perot and Mach–Zehnder interferometers based on hollow optical fiber fabricated by arc fusion splicing with small lateral offsets," *Opt. Commun.*, vol. 284, no. 22, pp. 5311–5314, Oct. 2011.

[18] P. Wang, G. Brambilla, M. Ding, Y. Semenova, Q. Wu, and G. Farrell, "High-sensitivity, evanescent field refractometric sensor based on a tapered, multimode fiber interference," *Opt. Lett.*, vol. 36, no. 12, pp. 2233–2235, Jun. 2011.

[19] S. Gao, W. Zhang, P. Geng, X. Xue, H. Zhang, and Z. Bai, "Highly sensitive in-fiber refractive index sensor based on down-bitaper seeded up-bitaper pair," *IEEE Photon. Technol. Lett.*, vol. 24, no. 20, pp. 1878–1881, Oct. 15, 2012.

[20] X. Wen et al., "Dumbbell-shaped Mach–Zehnder interferometer with high sensitivity of refractive index," *IEEE Photon. Technol. Lett.*, vol. 25, no. 18, pp. 1839–1842, Sep. 15, 2013.

[21] J. Chen, J. Zhou, and X. Yuan, "M–Z interferometer constructed by two S-bend fibers for displacement and force measurements," *IEEE Photon. Technol. Lett.*, vol. 26, no. 8, pp. 837–840, Apr. 15, 2014.